Measurement range of phase retrieval in optical surface and wavefront metrology

Gregory R. Brady* and James R. Fienup

The Institute of Optics, University of Rochester, Wilmot Building Room 121, Rochester, New York 14627, USA

*Corresponding author: grbrady@gmail.com

Received 3 July 2008; revised 31 October 2008; accepted 9 December 2008;
posted 10 December 2008 (Doc. ID 98290); published 12 January 2009

Phase retrieval employs very simple data collection hardware and iterative algorithms to determine the phase of an optical field. We have derived limitations on phase retrieval, as applied to optical surface and wavefront metrology, in terms of the speed of beam (i.e., f-number or numerical aperture) and amount of aberration using arguments based on sampling theory and geometrical optics. These limitations suggest methodologies for expanding these ranges by increasing the complexity of the measurement arrangement, the phase-retrieval algorithm, or both. We have simulated one of these methods where a surface is measured at unusual conjugates. © 2009 Optical Society of America

OCIS codes: 100.5070, 120.5050, 120.3940, 120.6650, 120.3930, 220.4840.

1. Introduction

Phase retrieval is a method of estimating the phase of an optical field from measurements of the intensity of the field propagated to one or more planes where the beam can be collected by a detector array, typically at or near focus where the light can be captured by the detector array. An idealized schematic of the collection method is shown in Fig. 1. A phase-retrieval algorithm iteratively searches for a phase estimate that defines an optical field that, when digitally propagated to the measurement planes, has intensity distributions in agreement with the measured intensities. The method has been successfully employed in the past for image recovery [1–3], wavefront sensing for adaptive optics [4], and for diagnosing the aberrations of the Hubble Space Telescope [5,6]. It will be used to align the segments of the James Webb Space Telescope [7]. It has not, however, been widely used to measure optical systems and surfaces during manufacturing.

Phase retrieval shows promise as an optical shop testing tool in certain applications. The experimental arrangements involved are often simpler and, hence, less expensive, than conventional interferometric arrangements, particularly for the measurement of concave surfaces or positive powered elements or systems in transmission. Since the measurement is not relative to a reference path, it is inherently tolerant of vibration effects that degrade the accuracy of interferometry. Aspheric wavefronts or surfaces can be measured without the retrace or imaging errors that are problematic in nonnull aspheric testing in most interferometers. By retrace errors, we mean errors in double-pass interferometry where the ray paths to and from the aspheric surface under test are different due to the nonnormal incidence of the rays on the aspheric surface. By imaging errors, we refer to errors in imaging the aspheric wavefront in the plane of incidence to the plane of the interferometer's detector array. An interferometer capable of testing concave aspheric parts without retrace errors has been demonstrated but is more complex than the equivalent phase-retrieval arrangement [8].

In an emerging method such as phase retrieval, it is important to define a measurement space in which the technique may be applicable. Here we derive the degree to which phase retrieval is limited by (1) the speed [i.e., f-number or numerical aperture (NA)] of the converging beam that forms the measured intensity pattern, (2) the pixel pitch of the detector array,

0003-6935/09/030442-08$15.00/0

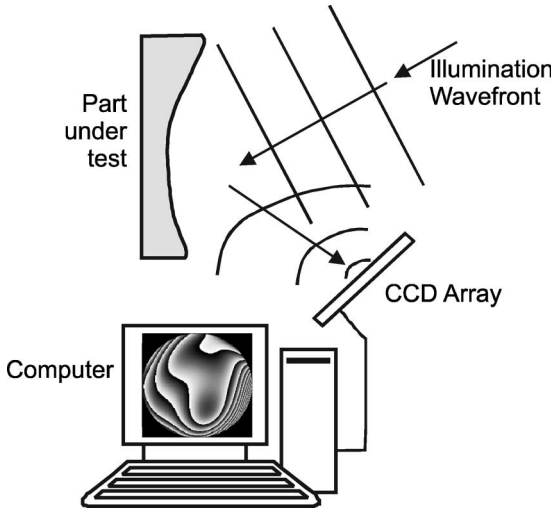

Fig. 1. Sketch showing the key components required for phase-retrieval-based optical metrology.

(3) the maximum slope of the nonspherical wavefront that is being measured, and (4) the diameter of the detector array. These limits are used to quantify ranges of these parameters over which the simplest embodiment of phase retrieval can be employed. We also discuss methods that can be used to increase these ranges by increasing the complexity of the experimental arrangement or the phase-retrieval algorithm.

2. Limitation on Speed of Beam

A. Sampling Limitation

The speed of the beam that can be measured using phase retrieval can be determined by a sampling consideration. Suppose that we are using a discrete version of the Fresnel diffraction integral to propagate the numerical field in the pupil (x) plane to the measurement (ξ) plane employing a discrete Fourier transform [computed using a fast Fourier transform (FFT)]. Then the relationship between the sample spacing, d_x and d_ξ, respectively, in the planes is given by [5,9]

$$d_\xi = \frac{\lambda z}{N d_x}, \tag{1}$$

where λ is the wavelength, N is the number of samples across the array of data in the pupil plane, and z is the propagation distance. The sampling of the intensity data can be described by the relation

$$N d_x = Q D, \tag{2}$$

where D is the diameter of the pupil,

$$Q = \frac{\lambda z}{d_\xi D} = \frac{\lambda f/\#}{d_\xi} \tag{3}$$

is the sampling ratio, $f/\# = z/D$ is the f-number, and the quantity $N d_x$ defines the spatial region over which the pupil plane is represented in the computer. A value of $Q = 2$ corresponds to Nyquist sampling of the intensity pattern (in which case the pupil diameter in pixels is half the array width N), $Q = 1$ corresponds to Nyquist sampling of the underlying field, and a value of $Q < 1$ means that the data is undersampled for both intensity and field. If we define a minimum value of Q for the sampling criteria that we are using, $Q_{\min}$, so that $Q \geq Q_{\min}$, and rearranging Eq. (3) as $f/\# = Q d_\xi/\lambda$, we arrive at a limit on the minimum value of the f-number:

$$f/\# \geq \frac{Q_{\min} d_\xi}{\lambda}. \tag{4}$$

We note that the sample spacing in the measurement plane, d_ξ, is a property of the detector array used. Using the usual approximate relation between the NA and the f-number, $\mathrm{NA} = 1/(2f/\#)$, we find an upper limit on the NA:

$$\mathrm{NA} \leq \frac{\lambda}{2 Q_{\min} d_\xi}. \tag{5}$$

The limiting cases of these relationships are plotted in Fig. 2 using a wavelength of 632.8 nm for Nyquist sampling of the field. Detector arrays with sample spacing of 3.5 μm are commercially available [10]. Using this sample spacing at a wavelength of 632.8 nm, the minimum f-number that can be measured is 5.5 when Nyquist sampling the field ($Q = 1$). The corresponding maximum NA that can be measured is 0.090. Hence, straightforward application of the phase-retrieval method is limited to testing moderately slow optics.

From Eq. (4) we see that the f-number limit can be reduced (or NA limit increased) by increasing the wavelength, reducing the (effective) sample spacing, or reducing $Q_{\min}$. Increasing the wavelength appreciably would require infrared detector arrays, which are less readily available and less refined than those in the visible. Infrared detector arrays typically have significantly larger pixel spacing d_ξ than visible light arrays, putting the use of infrared light at a disadvantage. Furthermore, since phase scales inversely with wavelength, wavefront measurements at longer wavelengths give one less sensitivity in terms of optical path differences. It would be useful to vary the other parameters to expand our measurement range. This is discussed in the following sections.

B. Magnification

While detector sample spacings are continually getting smaller in the race for more megapixels, the reduction is somewhat incremental. For an immediate improvement, a magnifying optical system, such as a microscope objective lens, can be used to magnify the intensity pattern onto the detector array, effectively decreasing the pixel size. If an objective with magnification m is employed, we can simply replace d_ξ by d_ξ/m, in Eqs. (4) and (5), giving the following limits on f-number and NA:

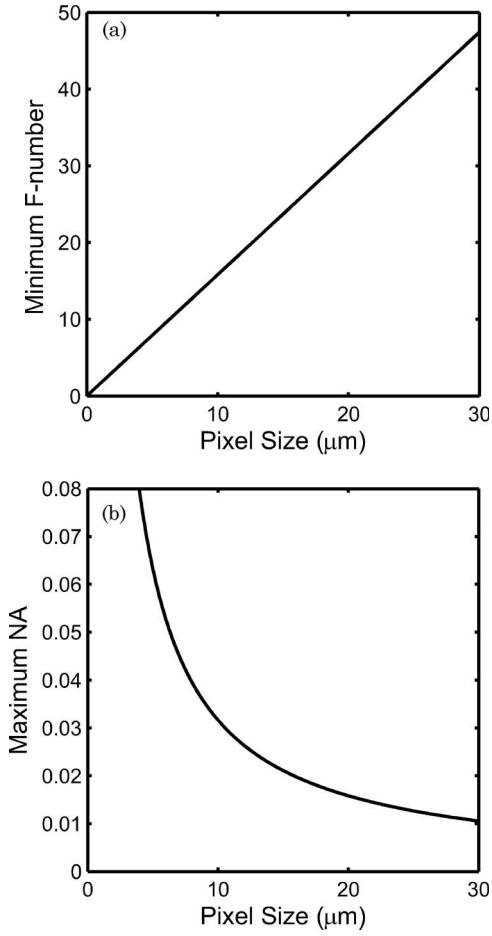

Fig. 2. (a) Plot of the minimum f-number and (b) maximum numerical aperture that can be measured using phase retrieval with a bare detector array, assuming a sampling parameter $Q_{\min} = 1$.

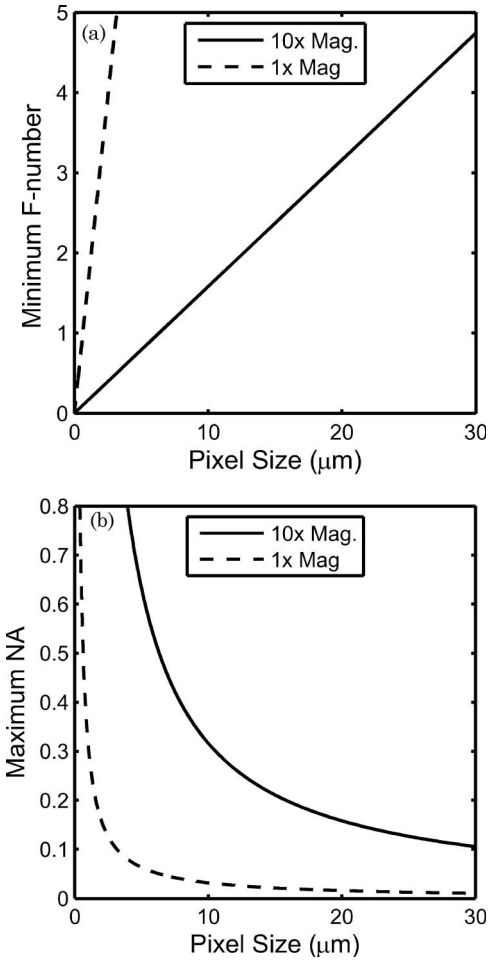

Fig. 3. (a) Plot of the minimum f-number and (b) maximum numerical aperture that can be measured using phase retrieval and an imaging optical system with a magnification of 10×, assuming a sampling parameter $Q_{\min} = 1$.

$$f/\# \geq \frac{Q_{\min} d_\xi}{m\lambda}, \tag{6}$$

$$\mathrm{NA} \leq \frac{m\lambda}{2Q_{\min} d_\xi}. \tag{7}$$

For example, if a magnifying power of 10× is employed, a factor of 10 improvement in the speed of the beam that can be measured is realized, as shown in Fig. 3.

Using a magnifying optical system has some drawbacks. The complexity of the experimental arrangement is increased and the aberrations of the magnifying system may introduce errors into the phase-retrieval results; particularly worrisome are field-dependent aberrations.

C. Stitching

A faster optic can be measured by sequentially measuring smaller subapertures of the optic (employing an aperture stop near the optic) and stitching the results together. The effective value of Q is inversely proportional to the diameter of the subaperture, allowing the minimum f-number to be driven by the subaperture diameter. The stitching task here is simpler than in subaperture stitching interferometry because no distortions due to an imaging system are present [11,12]. With stitching, the speed of the optics is not limited, but stitching requires additional hardware, data collection, and data processing.

D. Undersampling

With standard phase-retrieval algorithms it is possible to work at the Nyquist limit of the field ($Q = 1$) and produce good results. Specialized algorithms have been demonstrated that operate beyond the Nyquist limit [13], so that data with $Q < 1$ can be used. This approach is very attractive because no additional hardware is required. However, the accuracy of algorithms working in this regime has not been adequately explored.

E. Subpixel Dithering

By taking multiple exposures with different translations of the detector array by a fraction of d_ξ, it is possible to reconstruct the intensity pattern at a finer

effective sample spacing [14] and thereby decrease the allowable f-number. However, the accuracy of retrieving phase using this technique has not been adequately explored.

F. Use of Different Conjugates

It is often possible to change the conjugates that are used in the test to create a beam that is slow enough to be adequately sampled by the detector array. Here we consider the example of a concave spherical surface tested in reflection. Similar analyses can be performed for more complex systems.

The usual method of testing such a surface would place a point source at the center of curvature of the sphere. The beam reflected off the sphere converges back to the center of curvature, producing a beam with an f-number equal to the "R-number" of the surface:

$$R/\# = \frac{|R_c|}{D}, \tag{8}$$

where R_c is the radius of curvature of the surface. In a practical arrangement, a beamsplitter would be required to gain access to this focused spot, which could introduce wavefront errors. To avoid a beamsplitter, the mirror could be tilted slightly, introducing astigmatism. To increase the f-number for a given R-number, the measurement conjugates could be changed, introducing spherical aberration.

If we move the point source closer to the surface, as illustrated in Fig. 4(a), the image of the point source moves farther from the surface, producing a slower beam, according to the Gaussian image formation equation

$$-\frac{2}{R_c} = -\frac{1}{l} + \frac{1}{l'}, \tag{9}$$

where l is the object distance and l' is the image distance. In our sign convention, R_c, l, and l' are all negative for the geometry shown in Fig. 4(a) and R_c and l are positive while l' is negative in the geometry shown in Fig. 4(b). The image-space f-number is then $-l'/D$ in either case. If we multiply both sides of (9) by D and rearrange, making use of the relation for the f-number, we have

$$f/\# = \left(\frac{-2D}{R_c} + \frac{D}{l}\right)^{-1}. \tag{10}$$

We can now determine a range of object distances l that give adequately sampled data. This range has limits defined by inserting Eq. (10) into Eq. (6) and solving for l. Furthermore, no real image is formed at a finite conjugate when the object is at or inside the focal point (where $l = R_c/2$). The range is then

$$\left(\frac{m\lambda}{Q_{\min} D d_\xi} + \frac{2}{R_c}\right)^{-1} \le l < \frac{R_c}{2}. \tag{11}$$

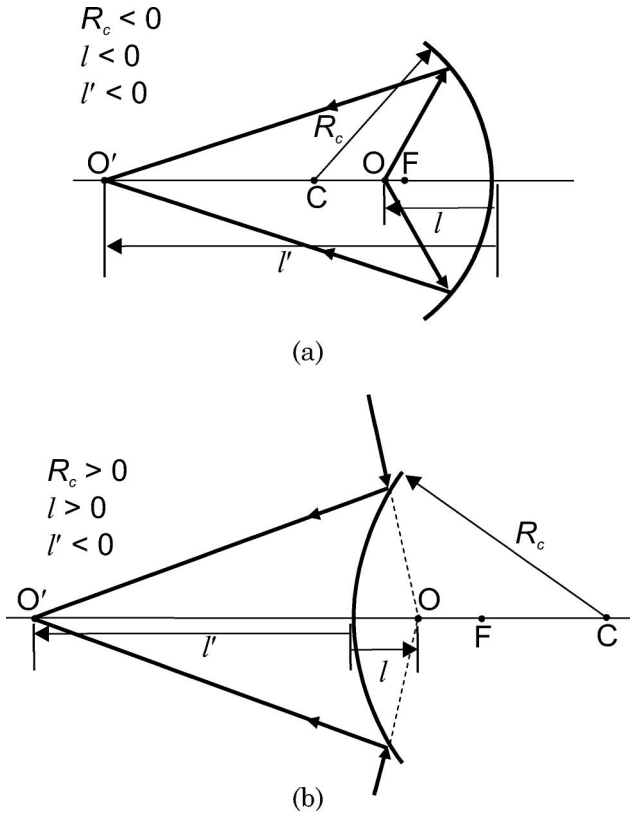

Fig. 4. Sketches of arrangements where a point source is placed at object point O and is imaged to image point O′ using the (a) convex and (b) concave spherical surfaces under test to form a converging beam that can be adequately sampled. Point F is the focus of the surface and point C is the center of curvature of the surface. Distances l and l' are the object and image distances, and R_c is the radius of curvature of the surface.

Note that if the center of curvature of the surface falls within this range, we would almost certainly choose to place the point source there because of the aberration-free imaging, but as stated above, a beamsplitter or small tilt of the optic would be required to gain access to the image.

This technique is not as attractive for the measurement of convex surfaces. An auxiliary optic would be necessary to form the required converging wavefront and must focus the beam to a (virtual) object point, as defined by Eq. (11), necessarily inside the focal point of the surface. However, traditional methods for testing a concave surface use an optic to focus the test beam to the center of curvature of the surface. Thus, in this arrangement, the test beam must converge at least twice as quickly as in the traditional methods.

Another drawback of using different conjugates is that it induces spherical aberration in the measured wavefront that is due only to the choice of conjugates. The bulk of the aberration is third-order spherical, which can be calculated in a straightforward manner and, in principle, removed from the measurement. As derived in Appendix A, the amount of third-order aberration is given by

$$W_{040} = \begin{cases} \frac{D}{64R/\#}\left(\frac{1}{f/\#} - \frac{1}{R/\#}\right)^2 & \text{concave } (R_c < 0) \\ -\frac{D}{64R/\#}\left(\frac{1}{f/\#} + \frac{1}{R/\#}\right)^2 & \text{convex } (R_c > 0). \end{cases} \tag{12}$$

Practical limitations on the measured aberration from this technique are defined in Section 3. It is also important to consider that the wavefront or surface errors of interest here become comparatively small perturbations to a very large spherical aberration term. To determine whether these errors can be measured with acceptable precision or accuracy, we performed computer simulations of phase retrieval, incorporating realistic noise and quantization errors. In this example, we simulated the measurement of a concave mirror with a diameter of 100 mm and a radius of curvature of 341.4 mm. This corresponds to an R-number of 3.41. If we desire the f-number of the measurement beam to be 33.3 in order to adequately sample the beam, then $W_{040} = 50\lambda$ at $\lambda = 632.8$ nm. The point source would be placed 162.4 mm in front of the concave mirror, producing an image focus 3333 mm in front of the mirror. The simulation used measurements from two planes, 30 and 60 mm inside the image focus. A sketch of this arrangement is shown in Fig. 5. A square detector array with $N = 1024$ and $d_\xi = 7.4\,\mu$m was modeled. Poisson noise corresponding to a peak pixel well containing 24,000 photoelectrons was added to each simulated image, as well as Gaussian noise with a standard deviation of 16 photoelectrons. The images were quantized to 12 bits. In addition, in each plane, two images with different exposure levels were simulated so that detail in regions with poor signal-to-noise ratio can be distinguished from background. Portions of the longer exposure images are saturated, but only data from the unsaturated regions of these images is used by the algorithm. Conversely, in the shorter exposure images, only regions that are saturated in the longer exposure images are used by the algorithm. As demonstrated in Fig. 6, a wavefront with an error of 0.2 waves peak to valley (0.05 waves RMS) riding on a nominal wavefront with 50 waves peak to valley (14.9 waves RMS) of primary spherical aberration can be retrieved to an accuracy of 0.0054 waves RMS or 0.026 wave peak to valley.

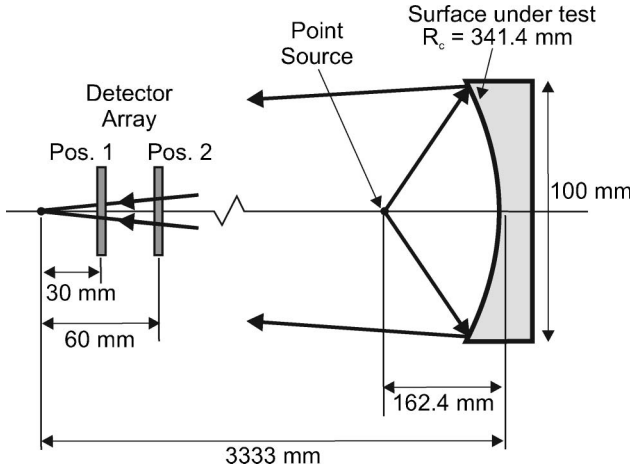

Fig. 5. Sketch of arrangement simulated. A point source is placed 162.4 mm in front of a concave surface with a radius of curvature of 341.4 mm and diameter of 100 mm. The point source is imaged to a point 3333 mm in front of the mirror. A detector array is used to measure the intensity pattern in two planes 30 and 60 mm inside the image plane.

3. Limit on Aberrations

A. Basic Aberration Limitation

The limit on the amount of aberration that can be measured can be derived from the requirement that the aberrated blur spot predicted by geometric optics must fall entirely on the detector array. The validity of this requirement arises from the fact that geometric optics effects dominate when determining the shape of a highly aberrated spot. The transverse aberrations are related to the slope of the wavefront [15], so this requirement can be written as

$$Nd_\xi \geq \frac{2z}{D}\left\{\left[\frac{\partial W(\rho)}{\partial \rho}\right]_{\max} - \left[\frac{\partial W(\rho)}{\partial \rho}\right]_{\min}\right\}, \tag{13}$$

where ρ is the transverse pupil coordinate normalized to unity at $D/2$. The derivatives on the right-hand side of the inequality represent the maximum slope difference between points on the wavefront. The quantity $2z/D$ scales the wavefront slope to give the lateral size of the blur spot. The left hand side of the inequality represents the physical size of the detector array, simply the product of the number of detector elements N multiplied by the element spacing d_ξ. Rearranging Eq. (13) and recognizing that $z/D = f/\#$, we have an upper limit on the maximum allowable slope difference:

$$\left[\frac{\partial W(\rho)}{\partial \rho}\right]_{\max} - \left[\frac{\partial W(\rho)}{\partial \rho}\right]_{\min} \leq \frac{Nd_\xi}{2f/\#}. \tag{14}$$

If we make use of our lower limit on f-number from Eq. (4), the maximum slope difference that can be measured is

$$\left[\frac{\partial W(\rho)}{\partial \rho}\right]_{\max} - \left[\frac{\partial W(\rho)}{\partial \rho}\right]_{\min} \leq \frac{\lambda N}{2Q_{\min}}. \tag{15}$$

This can be further simplified by realizing that a linear phase term (i.e., tip or tilt) can be introduced to the wavefront so that $[\partial W(\rho)/\partial\rho]_{\min} = -[\partial W(\rho)/\partial\rho]_{\max}$. This is equivalent to positioning the detector so that the rays corresponding to these slopes fall at the same distance from the center of the detector. The resulting expression is then

$$\left[\frac{\partial W(\rho)}{\partial \rho}\right]_{\max} \leq \frac{\lambda N}{4Q_{\min}}. \tag{16}$$

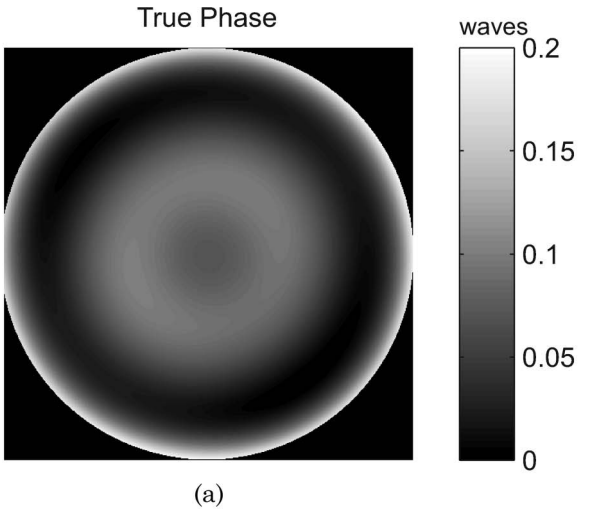

Fig. 6. Simulation of a phase-retrieval result for a wavefront whose nominal shape includes 50 waves of spherical aberration. The wavefronts shown have the spherical aberration term removed and only the residual errors that are of interest are shown. The scales to the right are in units of waves. (a) The true wavefront used in the simulation, (b) the recovered wavefront, and (c) the difference between the true wavefront and the recovered wavefront, having an RMS of 0.0054 waves and a PV of 0.026 waves.

It is interesting to compare this limit to the limit imposed in interferometry by the requirement of Nyquist sampling the fringe pattern. The normalized intensity pattern produced by a wavefront in an ideal interferometer is given by the expression

$$I(\rho) = \frac{1}{2}\left\{1 + \cos\left[\frac{2\pi}{\lambda}W(\rho)\right]\right\}. \tag{17}$$

Two samples per fringe period are required to Nyquist sample this intensity pattern or, in other words, there can be no more than π radians of phase difference between adjacent pixels:

$$\frac{2\pi}{\lambda}|W(\rho + \Delta\rho) - W(\rho)|_{\max} \le \pi, \tag{18}$$

where $\Delta\rho$ is the size of a pixel in the normalized coordinates. If $\Delta\rho$ is small, the left-hand side of Eq. (18) can be written as

$$\frac{2\pi}{\lambda}\left[\left|\frac{\partial W(\rho)}{\partial\rho}\right|_{\max}\Delta\rho\right] \le \pi. \tag{19}$$

In the normalized coordinate system we are using, $\Delta\rho = 2/N$. The maximum magnitude of the slope is thus

$$\left|\frac{\partial W(\rho)}{\partial\rho}\right|_{\max} \le \frac{\lambda N}{4}. \tag{20}$$

This limit is identical to the one derived for phase retrieval in Eq. (16) if we Nyquist sample the field ($Q_{\min} = 1$). That these two vastly different measurement techniques yield an identical limit is interesting indeed. Despite this equivalence, phase retrieval may still be useful for measuring aspherical wavefronts because of its simplicity and because it does not suffer from retrace errors present in dual-pass interferometers or from errors associated with imaging nonspherical wavefronts present in most interferometers. We note that not all interferometric arrangements suffer from these errors [8].

Consider a numerical example of the slope limitation for the case where a wavefront with a large amount of Seidel spherical aberration is to be measured. The form of this wavefront is

$$W(\rho) = W_{040}\rho^4, \tag{21}$$

where W_{040} is the Seidel coefficient of spherical aberration. It is relatively simple to show that some defocus, W_{020}, can be introduced to minimize the size of the geometric blur. The amount of defocus that minimizes the geometric spot size is $W_{020} = (-3/2)W_{040}$. This can be achieved by a small longitudinal movement of the detector array. The wavefront of interest would then be

$$W(\rho) = W_{040}\left(\rho^4 - \frac{3}{2}\rho^2\right). \tag{22}$$

Evaluating the derivative in Eq. (16), we have

$$\left[\frac{\partial W(\rho)}{\partial \rho}\right]_{\max} = W_{040}. \tag{23}$$

Substituting this result gives an upper limit on spherical aberration:

$$W_{040} \le \frac{\lambda N}{4Q_{\min}}. \tag{24}$$

If our detector array has $N = 1024$ elements and we Nyquist sample the field ($Q_{\min} = 1$), the maximum spherical aberration that can be measured is 256λ. If this wavefront is formed by an aspheric surface, this would be equivalent to a departure from the best fit spherical surface of about 32λ or $20\,\mu$m.

The result in Eq. (24) is true only for the functional form of the wavefront assumed in Eq. (22); however, it is straightforward to derive similar expressions for other wavefronts, including those parameterized using Zernike polynomials.

B. Magnification

If a magnifying (or demagnifying) optical system is used to image the diffraction spot, then Eq. (14) can be written (using $[\partial W(\rho)/\partial\rho]_{\min} = -[\partial W(\rho)/\partial\rho]_{\max}$ as above)

$$\left[\frac{\partial W(\rho)}{\partial \rho}\right]_{\max} \le \frac{N d_\xi}{4mf/\#}. \tag{25}$$

So, if we are able to fix the f-number, demagnifying the diffraction spot will increase the maximum wavefront slope that can be measured. However, to define a limit, we wish to use the minimum possible f-number, given in Eq. (6). Note that the magnification is present in the denominator of Eq. (6), so that resulting maximum slope possible is still given by

$$\left[\frac{\partial W(\rho)}{\partial \rho}\right]_{\max} \le \frac{N\lambda}{4Q_{\min}}, \tag{26}$$

regardless of the magnification. However, a benefit can be achieved using demagnification together with either undersampling or dithering. If a spot is initially critically sampled, but does not fit on the detector array, demagnification could be used to make the spot smaller. The spot would then be undersampled; in other words, the factor $Q_{\min}$ in Eq. (26) would decrease. Using a phase-retrieval algorithm that handles undersampled data, as in Section 2.D, or dithering the detector array, as in Section 2.E, could be used to effectively reduce $Q_{\min}$.

C. Extending Range of Wavefront Measurement Using Subaperture Stitching

As we mentioned above, stitching together multiple measurements can be used to increase the f-number range of a measurement. It can similarly be used to increase the aberrations that we can measure using phase retrieval, since the left-hand side of Eq. (14) will typically be smaller over a given subaperture. Again, this is similar to subaperture stitching interferometric techniques [11], but would be simpler because retrace and imaging errors do not need to be corrected.

D. Extending Range of Wavefront Measurement by Stitching the Intensity Pattern

The limit of the aberrations that can be measured is determined by the largest spot size that does not overfill the detector array. In this situation, it should be possible to mount the detector on a translation stage moving in the lateral directions and make multiple translated measurements of the intensity pattern. These measurements could then be stitched together to form a larger effective detector array. This would increase the amount of data to be processed and increase the measurement time, processing time, and memory requirements, but would increase the largest slope deviation.

4. Conclusion

We have quantified the limitations on the range of phase retrieval for a given detector array and wavelength. We have also shown that the simplest embodiments of phase retrieval are most useful for the testing of concave surfaces or positive powered transmissive parts. The speed of the beam to be measured is primarily limited by the pixel pitch of the detector array, while the maximum wavefront slope is principally limited by the size of the detector array. The simplest phase-retrieval arrangement, consisting of free-space propagation to a bare detector array, is capable of measuring beams of f-numbers greater than $f/5.5$ (NAs smaller than 0.090) with current detector technology having $3.5\,\mu$m pixel pitch. Magnifying optics, detector dithering, undersampling, and choosing appropriate conjugates can all be used to measure faster beams. A 1024 element detector array could measure up to 256 waves of spherical aberration in this simplest arrangement. This limit can be increased using demagnification, together with dithering or undersampling, by stitching subaperture wavefront measurements together, or by stitching together raw intensity measurements to produce a larger effective detector array.

Appendix A

For the arrangements shown in Figs. 4(a) and 4(b), the spherical aberration can be calculated using the first Seidel sum [16]:

$$S_1 = -\sum_{\text{surfaces}} A^2 y_a \left(\frac{u'_a}{n'} - \frac{u_a}{n}\right), \tag{A1}$$

where y_a is the marginal ray height, u_a and u'_a are the paraxial marginal ray angles before and after the surface, respectively, and n and n' are the indices of refraction before and after the surface (1 and −1 here). The quantity A is given by

$$A = n i_a, \tag{A2}$$

where i_a is the incident angle of the marginal ray. The Seidel sum is related to the primary spherical aberration coefficient by the relationship

$$W_{040} = \frac{1}{8} S_1. \tag{A3}$$

The marginal ray angle before the surface is given by

$$u_a = \frac{-D/2}{l}. \tag{A4}$$

The marginal ray angle after the surface is given by

$$n' u'_a = n u_a - y_a \frac{-2}{R_c}. \tag{A5}$$

Solving for the marginal ray angle, we have

$$u'_a = D\left(\frac{1}{2l} - \frac{1}{R_c}\right). \tag{A6}$$

The incident angle at the surface can be calculated using

$$i_a = u_a + \frac{y_a}{R_c} = \frac{D}{2}\left(\frac{1}{R_c} - \frac{1}{l}\right). \tag{A7}$$

Using the above relations, the spherical aberration coefficient is then

$$W_{040} = -\frac{D^4}{64 R_c}\left(\frac{1}{R_c} - \frac{1}{l}\right)^2, \tag{A8}$$

which can equivalently be written in terms of the image distance

$$W_{040} = -\frac{D^4}{64 R_c}\left(\frac{1}{l'} + \frac{1}{R_c}\right)^2, \tag{A9}$$

or in terms of the object space f-number ($f/\# = -l'/D$) and the R-number ($R/\# = |R_c|/D$):

$$W_{040} = \begin{cases} \frac{D}{64R/\#}\left(\frac{1}{f/\#} - \frac{1}{R/\#}\right)^2 & \text{concave } (R_c < 0) \\ -\frac{D}{64R/\#}\left(\frac{1}{f/\#} + \frac{1}{R/\#}\right)^2 & \text{convex } (R_c > 0). \end{cases} \tag{A10}$$

The support of QED Technologies, Corning Tropel Corporation and the Center for Electronic Imaging Systems (CEIS)/New York State Office of Science, Technology, and Academic Research (NYSTAR) is gratefully acknowledged.

References

1. R. W. Gerchberg and W. O. Saxton, "A practical algorithm for the determination of the phase from image and diffraction plane pictures," Optik (Jena) **35**, 237–246 (1972).
2. J. R. Fienup, "Reconstruction of an object from the modulus of its Fourier transform," Opt. Lett. **3**, 27–29 (1978).
3. J. N. Cederquist, J. R. Fienup, J. C. Marron, and R. G. Paxman, "Phase retrieval from experimental far-field data," Opt. Lett. **13**, 619–621 (1988).
4. J. N. Cederquist, J. R. Fienup, C. C. Wackerman, S. R. Robinson, and D. Kryskowski, "Wave-front phase estimation from Fourier intensity measurements," J. Opt. Soc. Am. A **6**, 1020–1026 (1989).
5. J. R. Fienup, "Phase-retrieval algorithms for a complicated optical system," Appl. Opt. **32**, 1737–1746 (1993).
6. J. R. Fienup, J. C. Marron, T. J. Schulz, and J. H. Seldin, "Hubble space telescope characterized by using phase retrieval algorithms," Appl. Opt. **32**, 1747–1768 (1993).
7. B. H. Dean, D. L. Aronstein, J. S. Smith, R. Shiri, and D. S. Acton, "Phase retrieval algorithm for JWST flight and testbed telescope," Proc. SPIE **6265**, 626511 (2005).
8. G. E. Sommargren, D. W. Phillion, M. A. Johnson, N. Q. Nguyen, A. Barty, F. J. Snell, D. R. Dillon, and L. S. Bradsher, "100-picometer interferometry for EUVL," Proc. SPIE **4688**, 316–28 (2002).
9. Joseph W. Goodman, *Introduction to Fourier Optics*, 3rd ed. (Roberts, 2003), Chap. 9.
10. For example, the Sony ICX625 CCD Image Sensor.
11. P. Dumas, J. Fleig, G. Forbes, and P. E. Murphy, "Extending the range of interferometry through subaperture stitching," Proc. SPIE **TD02**, 134–7 (2003).
12. M. Bray, "Stitching interferometer for large optics using a standard interferometer: description of an automated system [for ICF optics]," Proc. SPIE **3047**, 911–18 (1997).
13. J. R. Fienup, "Phase retrieval for undersampled broadband images," J. Opt. Soc. Am. A **16**, 1831–1839 (1999).
14. S. C. Park, M. K. Park, and M. G. Kang, "Super-resolution image reconstruction: a technical overview," IEEE Signal Process. Mag. **20**, 21–36 (2003).
15. W. T. Welford, *Aberrations of Optical Systems* (Taylor & Francis, 1986), Chap. 7.
16. W. T. Welford, *Aberrations of Optical Systems* (Taylor & Francis, 1986), Chap. 8.